Lawrence Berkeley National Laboratory
LBL Publications

Title
A Search for Correlated Low-energy Electron Antineutrinos in KamLAND with Gamma-Ray Bursts

Permalink

Journal

ISSN

Authors
Abe, S
Asami, S
Gando, A
et al.

Publication Date

DOI

Peer reviewed

A Search for Correlated Low-energy Electron Antineutrinos in KamLAND with Gamma-Ray Bursts

S. Abe[1], S. Asami[1], A. Gando[1], Y. Gando[1], T. Gima[1], A. Goto[1], T. Hachiya[1], K. Hata[1], K. Hosokawa[1], K. Ichimura[1],
S. Ieki[1], H. Ikeda[1], K. Inoue[1,2], K. Ishidoshiro[1], Y. Kamei[1], N. Kawada[1], Y. Kishimoto[1,2], T. Kinoshita[1], M. Koga[1,2],
N. Maemura[1], T. Mitsui[1], H. Miyake[1], K. Nakamura[1], K. Nakamura[1], R. Nakamura[1], H. Ozaki[1,3], T. Sakai[1], H. Sambonsugi[1],
I. Shimizu[1], J. Shirai[1], K. Shiraishi[1], A. Suzuki[1], Y. Suzuki[1], A. Takeuchi[1], K. Tamae[1], M. Eizuka[1], M. Kurasawa[1], T. Nakahata[1],
S. Futagi[1], H. Watanabe[1], Y. Yoshida[1], S. Obara[4], A. K. Ichikawa[5], S. Yoshida[6], S. Umehara[7], K. Fushimi[8], B. E. Berger[2,9],
B. K. Fujikawa[2,9], J. G. Learned[10], J. Maricic[10], S. N. Axani[11], J. Smolsky[11], C. Laber-Smith[11], L. A. Winslow[11], Z. Fu[11],
J. Ouellet[11], Y. Efremenko[2,12], H. J. Karwowski[13,14], D. M. Markoff[13,15], W. Tornow[2,13,16], A. Li[14], J. A. Detwiler[2,17],
S. Enomoto[2,17], M. P. Decowski[2,18], C. Grant[19], H. Song[19], T. O'Donnell[20], and S. Dell'Oro[20]
(KamLAND Collaboration)

[1] Research Center for Neutrino Science, Tohoku University, Sendai 980–8578, Japan
[2] Institute for the Physics and Mathematics of the Universe, The University of Tokyo, Kashiwa 277–8568, Japan
[3] Graduate Program on Physics for the Universe, Tohoku University, Sendai 980-8578, Japan
[4] Frontier Research Institute for Interdisciplinary Sciences, Tohoku University, Sendai 980–8578, Japan
[5] Department of Physics, Tohoku University, Sendai 980-8578, Japan
[6] Graduate School of Science, Osaka University, Toyonaka, Osaka 560-0043, Japan
[7] Research Center for Nuclear Physics (RCNP), Osaka University, Ibaraki, Osaka 567-0047, Japan
[8] Graduate School of Advanced Technology and Science, Tokushima University, Tokushima 770–8506, Japan
[9] Nuclear Science Division, Lawrence Berkeley National Laboratory, Berkeley, CA 94720, USA
[10] Department of Physics and Astronomy, University of Hawaii at Manoa, Honolulu, HI 96822, USA
[11] Massachusetts Institute of Technology, Cambridge, MA 02139, USA; saxani@mit.edu
[12] Department of Physics and Astronomy, University of Tennessee, Knoxville, TN 37996, USA
[13] Triangle Universities Nuclear Laboratory, Durham, NC 27708, USA
[14] The University of North Carolina at Chapel Hill, Chapel Hill, NC 27599, USA
[15] North Carolina Central University, Durham, NC 27701, USA
[16] Department of Physics, Duke University, Durham, NC 27705, USA
[17] Center for Experimental Nuclear Physics and Astrophysics, University of Washington, Seattle, WA 98195, USA
[18] Nikhef and the University of Amsterdam, Science Park, Amsterdam, The Netherlands
[19] Boston University, Boston, MA 02215, USA
[20] Center for Neutrino Physics, Virginia Polytechnic Institute and State University, Blacksburg, VA 24061, USA

Abstract

We present the results of a time-coincident event search for low-energy electron antineutrinos in the KamLAND detector with gamma-ray bursts (GRBs) from the Gamma-ray Coordinates Network and Fermi Gamma-ray Burst Monitor. Using a variable coincidence time window of $\pm 500\,\mathrm{s}$ plus the duration of each GRB, no statistically significant excess above the background is observed. We place the world's most stringent 90% confidence level upper limit on the electron antineutrino fluence below 17.5 MeV. Assuming a Fermi–Dirac neutrino energy spectrum from the GRB source, we use the available redshift data to constrain the electron antineutrino luminosity and effective temperature.

Unified Astronomy Thesaurus concepts: Gamma-ray bursts (629); Cosmological neutrinos (338)

1. Introduction

While gamma-ray bursts (GRBs) represent some of the most luminous electromagnetic sources of radiation in the known universe, their progenitors have long been a mystery. This has been partially resolved with the recent observation of a gravitational-wave signal (GW170817) correlated with the nearest observed GRB to date (GRB170817A) (Abbott et al. 2017a, 2017b), appearing to confirm the hypothesis that the class of "short" GRBs (SGRB) originate from binary mergers (Nakar 2007). The class of "long" GRBs (LGRB), by comparison, are found in host galaxies with more active star formation and are thought to result from the core collapse of

massive stars, exemplified by the correlated observation of GRB 130427A with SN 2013cq (Xu et al. 2013). In either case, the progenitors are expected to release copious amounts of energy in the form of neutrinos ($\mathcal{O}(10^{53}\,\mathrm{erg})$). The neutrino emission from the toroidal accretion disk surrounding the remnant of the binary star merger is expected to be the dominant source of MeV-scale neutrinos (Rosswog & Liebendoerfer 2003; Setiawan et al. 2006), with a subdominant flux contribution from the hot dense remnant itself (Ruffert & Janka 2001). This mechanism is similar to the models that also produce neutrinos in Type II supernovae, although the neutron-rich environment of the binary star merger is expected to produce a larger electron antineutrino ($\bar{\nu}_e$) flux (Rosswog & Liebendoerfer 2003).

The Kamioka Liquid scintillator Anti Neutrino Detector (KamLAND) has previously searched for astrophysical neutrinos associated with gravitational waves (Gando et al. 2016a; Abe et al. 2021), solar flares (Abe et al. 2022a), and
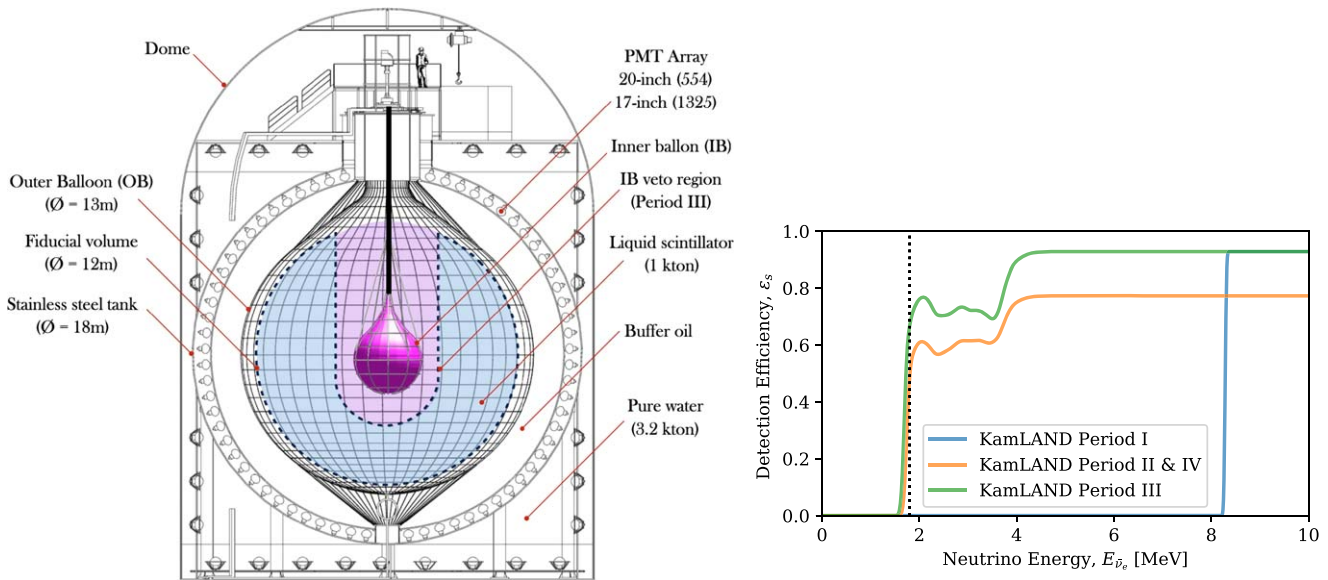
Figure 1. Left: a schematic diagram of the KamLAND detector. The fiducial volume is highlighted in blue. We illustrate the azimuthally symmetric inner balloon cut for data periods II and IV in purple. Right: the IBD $\bar{\nu}_e$ selection efficiencies for the four KamLAND periods. The structure below $\sim$4 MeV arises from the likelihood selection. A vertical dotted line is shown at the 1.8 MeV low-energy IBD threshold. The nonzero efficiency below 1.8 MeV is a result of smearing due to the energy resolution of the KamLAND detector.

supernovae (Abe et al. 2022b). This paper represents an update to the KamLAND result presented in Asakura et al. (2015). Time-coincident GRBs with MeV-scale neutrinos searches have also been performed by the Super-Kamiokande (Fukuda et al. 2002), Borexino (Agostini et al. 2017), and the Sudbury Neutrino Observatory (SNO; Aharmim et al. 2014). High-energy neutrinos are also expected to accompany GRBs in the collimated jet structure that forms from accreting matter. These searches have been performed by the IceCube (Abbasi et al. 2009, 2010), ANTARES (Albert et al. 2017), AMANDA (Hughey & Taboada 2005), and Baikal (Avrorin et al. 2011) collaborations.

In this paper, we present the results of a search for $\bar{\nu}_e$ with energies ranging from $E_{\bar{\nu}_e} = 1.8$ to 100 MeV contained in the 4931.1 day livetime (8.6 kiloton yr) data set from KamLAND, coincident with 2795 LGRBs and 465 SGRBs. We then use the subset of GRBs that have a measured redshift to constrain the $\bar{\nu}_e$ source luminosity and effective temperature.

2. KamLAND Detector

A schematic diagram of the KamLAND neutrino detector is shown in Figure 1 (left). The detector itself is situated in Kamioka, Japan, approximately 1 km under the surface of Mt. Ikenoyama. The detector is divided into two major sections: the inner detector and the outer detector, separated by an 18.0 m diameter spherical stainless steel tank. The inner detector was optimized for low-energy $\bar{\nu}_e$ interactions, primarily to measure geoneutrinos and neutrino oscillations using reactor neutrinos (Araki et al. 2005; Abe et al. 2008; Gando et al. 2013).

Inside the inner detector, there is a 13.0 m diameter spherical balloon made of a five-layer ethylene vinyl alcohol (EVOH) and nylon film, 135 μm thick. This balloon holds 1000 tons $(1171 \pm 25\,\text{m}^3)$ of ultrapure liquid scintillator, which is by volume 80% dodecane $(\rho = 0.75\,\text{g cm}^{-3})$ and 20% pseudocumene $(\rho = 0.88\,\text{g cm}^{-3})$. The inner 12.0 m diameter region is used as the fiducial volume for $\bar{\nu}_e$ detection. Outside the balloon, the inner detector is filled with a buffer oil, which helps to filter out gamma radiation from radioactive impurities in the detector or

surrounding material. The outer shell of the inner detector holds an array of 1325 17 inch photomultipliers (PMT) and 554 20 inch PMTs pointed radially inwards. These PMTs provide a total detector photocathode coverage of 34%. The vertex resolution of reconstruction is $\sim$12 cm/$\sqrt{E\,(\text{MeV})}$, and the energy resolution is $\sim$6.4%/$\sqrt{E\,(\text{MeV})}$ (Gando et al. 2013).

The readout electronics are synchronized with the Global Positioning System (GPS) via a pulse-per-second trigger from a receiver placed outside the entrance to the Kamioka mine. Based on the uncertainty from the accuracy of the GPS system, signal transportation into the mine, optical/electrical signal conversion, and trigger system uncertainties, we estimate the total uncertainty in the absolute event time stamp in Kam-LAND to be $\mathcal{O}(100\,\mu\text{s})$.

From 2011 October to 2015 October, a tear-drop-shaped, 3.08 m diameter, 25 μm thick, nylon inner balloon was installed in the center of the detector. During this period, the inner balloon was filled with approximately 326 kg of ^{136}Xe loaded liquid scintillator for the KamLAND-Zen 400 neutrino-less double-beta-decay experiment (Gando et al. 2016b). From 2018 April onward, a larger (3.8 m diameter) inner balloon was inserted into the detector and filled with approximately 745 kg of enriched xenon (676 kg of ^{136}Xe) for the KamLAND-Zen 800 experiment (Gando et al. 2020, 2021).

3. Data Selection and Background Estimation

3.1. Electron Antineutrino Selection

We use the inverse beta-decay (IBD) reaction $(\bar{\nu}_e + p \rightarrow e^+ + n)$ to search for $\bar{\nu}_e$ interactions in the KamLAND detector. The selection criteria for these events are described in detail in Gando et al. (2013) and Abe et al. (2021). The IBD reaction has a threshold of $E_{\bar{\nu}_e} = 1.803$ MeV and creates a delayed-coincidence (DC) event pair, which can be identified by both the separation in time $(0.5\,\mu\text{s} \leqslant \Delta T \leqslant 1000\,\mu\text{s})$ and space separation $(\Delta R \leqslant 200\,\text{cm})$ between the prompt e^+ thermalization then annihilation and delayed neutron capture. The mean

capture time for the neutron is $207.5 \pm 2.8\,\mu s$. The DC identification method greatly suppresses backgrounds and allows for a high $\bar{\nu}_e$ detection efficiency. The prompt energy, E_p, is equal to the sum of the e^+ kinetic energy and its annihilation energies ($E_p = T_{e_+} + 2m_e$). We can relate the prompt energy to the incident neutrino through $E_{\bar{\nu}_e} = E_p + \delta E + T_n$. Here, T_n is the kinetic energy of the neutron and δE is equal to 0.782 MeV. The thermalization of the neutron is also contained in the prompt event; however, it is quenched and can be ignored for low energies ($E_{\bar{\nu}_e} < 20$ MeV). Therefore throughout this analysis, we will use

$$E_{\bar{\nu}_e} \approx E_p + \delta E. \qquad (1)$$

This approximation is sufficiently accurate for the results presented in this paper and represents an 10% bias at $E_{\bar{\nu}_e} = 100$ MeV (Asakura et al. 2015).

The delayed neutron in the DC pair interacts with a $^1\mathrm{H}(^{12}\mathrm{C})$ molecule to form a deuteron ($^{13}\mathrm{C}$) and 2.22 MeV (4.95 MeV) gamma-ray. We include a cut on the reconstructed delayed energy, E_d, such that $1.8\,\mathrm{MeV} \leqslant E_d \leqslant 2.6\,\mathrm{MeV}$ or $4.4\,\mathrm{MeV} \leqslant E_d \leqslant 5.6\,\mathrm{MeV}$.

An additional likelihood-based selection is used to distinguish $\bar{\nu}_e$ DC pairs from coincident background events. The likelihood selection accounts for the accidental coincidence rates, the outer detector refurbishment (Ozaki & Shirai 2017), the inner balloon installation (Gando 2020; Gando et al. 2021), and the status of some of the reactors in Japan. Details of this likelihood selection method are further described in Gando et al. (2013).

We include KamLAND IBD data spanning from the first GRB in the catalog, 2004 December 19, to the most recently verified KamLAND data-taking run, 2021 June 12, separated into four time periods. Period I: This period includes all KamLAND data prior to the installation of the KamLAND-Zen 400 inner balloon in 2011 October. The $\bar{\nu}_e$ selection includes a low-energy threshold of $E_p = 7.5$ MeV to reduce the Japanese nuclear reactor neutrino background. Following a major earthquake in 2011 March, the operation of all nuclear power plants in Japan was suspended, and therefore, all subsequent time periods in this analysis have a low-energy threshold of $E_p = 0.9$ MeV. Period II: This spans the time in which the inner balloon was inserted into the KamLAND detector for the KamLAND-Zen 400 experiment (2011 October–2015 October). Here, we include an additional geometric cut on the delayed event around the inner balloon to reduce backgrounds from the inner balloon material. The cut removes the central spherical 2.5 m radius region, extending to the top of the detector in a 2.5 m radius cylinder. Period III: This period begins at the time of removal of the KamLAND-Zen 400 inner balloon and spans the time up until the introduction of the KamLAND-Zen 800 inner balloon. Period IV: This is during the KamLAND-Zen 800 experiment and reintroduces the same geometric cut described in Period II.

The inner balloon geometric cuts for Periods II and IV are illustrated as the purple region in Figure 1 (left), while the IBD selection efficiency as a function of $\bar{\nu}_e$ energy for each time period is shown in Figure 1 (right). Above 10 MeV, the selection efficiencies converge to 92.9% and 77.4% for Periods I and III, and II and IV, respectively. The reduction in fiducial volume due to the geometric cuts for Periods II and IV are accounted for in the selection efficiencies rather than in the number of target nuclei.

3.2. GRB Event Selection

The GRB events are extracted from GRBWeb (Aguilar 2011), an online cataloging tool that parses the Gamma-ray burst Coordinate Network[21] (GCN) publicly available circulars and the Fermi Gamma-ray Burst Monitor[22] (GBM). The circulars archive reports from satellites such as SWIFT, Fermi, INTEGRAL, HETE-2, AGILE, Ulysses, Suzaku, and WIND/Konus, along with supplemental data from ground-based observatories. We require that each event has an absolute trigger time (t_{GRB}) and a measured GRB duration (t_{90}), which represents the time interval in which the integrated photon counts increase from 5% to 95% of the total counts. We separate the GRBs into two classes demarcated by their duration: GRBs with $t_{90} < 2$ s are labeled "short" (SGRBs), whereas those with $t_{90} \geqslant 2$ are "long" (LGRBs) (Kouveliotou et al. 1993). After imposing a quality check on the KamLAND data, ensuring that we do not include GRBs that arrive during the KamLAND detector deadtime (e.g., during calibration runs or nonstable operation), the final GRB event selection sample contains 2795 LGRBs and 465 SGRBs. Of these, 377 LGRBs and 34 SGRBs are found to have a measured redshift. We will refer to the sum of the LGRB and SGRB data sets as the "combined set." Of note, contrary to the classification scheme presented here, although GRB 170817A (mentioned in Section 1) had a measured duration of $t_{90} = 2.048$ s we have placed it in the SGRB data set. A full list of the GRBs used in this analysis can be found on our website.[23]

3.3. Background Estimation

The background rate is calculated independently for each of the four KamLAND periods. The IBD events that occur outside of the coincidence time window around each GRB are used to determine the uncorrelated background rate. In Period I, enforcing that $E_p > 7.5$ MeV, the background is dominated by long-lived spallation products and fast neutrons from cosmic-ray muons (Abe et al. 2010) and by neutral current (NC) atmospheric neutrino interactions. While this is also the dominant source of higher-energy neutrinos in Periods II–IV, the dominant neutrino sources below approximately 8 MeV are the Japanese nuclear reactor power plants and geoneutrinos from radioactive decays in Earth (primarily below 3.4 MeV). Other backgrounds include DC pairs induced by the decay of radioactive impurities, spallation-produced $^9\mathrm{Li}$ and $^8\mathrm{He}$ leading to a β-decay followed by a neutron capture (Abe et al. 2010), and alpha-induced $^{13}\mathrm{C}(\alpha,n)^{16}\mathrm{O}$ reaction in the liquid scintillator. Using the background rates in each period and the sum of all coincidence time windows, the expected number of background events is found to be 2.94 for the LGRBs and 0.47 for the SGRBs. The period-dependent background information is shown in Table 1.

4. Time-coincident Event Search

We perform a time-coincident analysis searching for IBD events that coincide with a predefined window size around each GRB. The window size for each GRB trigger time, t_{GRB}, is

---

Table 1
The Period-dependent Information Used in This Analysis

	Realtime (days)	Livetime (days)	ϵ_{live} (%)	$\bar{\nu}_e$ Counts	Short Gamma-Ray Bursts			Long Gamma-Ray Bursts		
					Counts	Window (hr)	Bkg. Exp.	Counts	Window (hr)	Bkg. Exp.
Period I	2487.4	1985.0	79.8	14	121	33.7	0.01	838	262.1	0.08
Period II	1474.0	1371.8	93.1	148	172	47.8	0.22	911	279.5	1.26
Period III	558.9	480.3	85.9	58	56	15.6	0.08	323	97.7	0.49
Period IV	1152.7	1094.0	94.9	132	116	32.3	0.16	723	221.9	1.12
Total	5673.0	4931.1	86.9	352	465	129.3	0.47	2795	861.2	2.94

Note. The livetime efficiency, ϵ_{live}, is defined as the ratio between the livetime and realtime. The total number of neutrinos observed per period, along with the information regarding the number of observed SGRBs and LGRBs, their total time windows, and the expected number of background events, is also shown.

defined such that

$$t_{\text{GRB}} - t_{\text{p}} < t_{\text{DC}} < t_{\text{GRB}} + t_p + t_{90}, \qquad (2)$$

where t_{DC} is the DC IBD event time and the variable t_{p} represents a predefined window size of ± 500 s. t_{p} is chosen to be sufficiently large to cover reasonable model-dependent time differences between the neutrino and photon production within the GRB, and the neutrino time-of-flight delay. The model-dependent time differences account for temporal effects from the source evolution, such as those originating from precursor activity (Lazzati 2005; Burns 2020), accretion disk evaporation lifetimes (Liu et al. 1996), and core-collapse and Kelvin–Helmholtz cooling phase timescales (Totani et al. 1998).

Due to the nonzero neutrino mass, a neutrino time-of-flight delay is expected relative to the photon travel time. Using the neutrino oscillation parameters from Esteban et al. (2020) and assuming the sum of the neutrino masses to be <1.2 eV, we calculate the most massive neutrino state to be <59 meV and conservatively set this to be the mass of $\bar{\nu}_e$. Then, using the base-ΛCDM cosmological parameters from Aghanim et al. (2020), the time-of-flight delay for a 1.8 MeV $\bar{\nu}_e$ from the most distant GRB (GRB 100205A, with a suspected redshift $z < 13$; Kim & Im 2012; Chrimes et al. 2019) is estimated to be approximately 129 s. Therefore, the $t_{\text{p}} = \pm 500$ s is considered conservative.

The sum of all time windows, from Equation (2), is found to be 861.2 hr for LGRBs, 129.3 hr for SGRBs. The breakdown between periods is shown in Table 1.

5. Results

We find a single coincident event between a long GRB, GRB 180413A, and a low-energy IBD interaction in KamLAND during Period III. This GRB was extracted from the Fermi GBM and found to have a duration of $t_{90} = 57.86 \pm 2.36$ s (Aguilar 2011). This LGRB does not have a measured redshift. The coincident $\bar{\nu}_e$ was found to have a prompt (delayed) energy of $E_{\text{p}} = 4.24 \pm 0.13$ MeV ($E_{\text{d}} = 2.28 \pm 0.10$ MeV) and arrived 191.3 s prior to GRB 180413A. This observation is consistent with the background expectation.

The 90% confidence level (C.L.) lower and upper limits on the number of GRB-correlated IBD events is calculated according to the Feldman–Cousins procedure (Feldman & Cousins 1998). For the LGRB, SGRB, and combined sets, we find the 90% C.L. intervals to be [0.0, 1.91], [0.0, 1.97], and [0.0, 1.64] signal events, respectively. The upper limits of each interval, N_{90}, can be used to place an upper limit on the $\bar{\nu}_e$

fluence per GRB:

$$F_{90} = \frac{N_{90}}{N_{\text{T}} \sum_{k=1}^{k=4} \epsilon_{\text{live}}^k N_{\text{GRB}}^k \int \sigma(E_{\bar{\nu}_e}) \lambda(E_{\bar{\nu}_e}) \epsilon_s^k(E_{\bar{\nu}_e}) dE_{\bar{\nu}_e}}, \qquad (3)$$

where $N_{\text{T}} = 5.98 \times 10^{31}$ is the number of target nuclei in the fiducial volume, $\sigma(E_{\bar{\nu}_e})$ is the IBD cross section (Strumia & Vissani 2003), and $\lambda(E_{\bar{\nu}_e})$ is the normalized $\bar{\nu}_e$ energy spectrum. The summation iterates over the periods k, where ϵ_{live}^k represent the livetime efficiencies, N_{GRB}^k are the number of observed GRBs, and ϵ_s^k are the selection efficiencies from Figure 1 (right). The $\bar{\nu}_e$ energy spectrum, $\lambda(E_{\bar{\nu}_e})$, is often modeled as a temperature-dependent Fermi–Dirac (FD) distribution with zero chemical potential for core-collapse supernovae and binary mergers (Horiuchi et al. 2009; Gando et al. 2016a):

$$\lambda(E_{\bar{\nu}_e}, T)_{\text{FD}} = \frac{1}{T^3 f_2} \frac{E_{\bar{\nu}_e}^2}{e^{(E_{\bar{\nu}_e}/T)} + 1}, \quad f_n = \int_0^\infty \frac{x^n}{e^x + 1} dx. \quad (4)$$

If we take the mean $\bar{\nu}_e$ energy to be $\langle E \rangle = 12.7$ MeV and set $T = \langle E \rangle / 3.15$, we find the 90% C.L. upper limit on the $\bar{\nu}_e$ fluence, integrating Equation (3) from 1.8 to 100 MeV, per GRB to be

$$F_{90}^{\text{LGRB}} = 1.03 \times 10^6 \text{ cm}^{-2}, \; F_{90}^{\text{SGRB}} = 6.27 \times 10^7 \text{ cm}^{-2},$$
$$F_{90}^{\text{Combined}} = 0.75 \times 10^6 \text{ cm}^{-2}.$$
$$(5)$$

Alternatively, without making any assumption on the $\bar{\nu}_e$ energy spectrum, we instead calculate the equivalent model-independent Greene's Function, $\Psi(E_{\bar{\nu}_e})$, comparable to Fukuda et al. (2002), by setting $\lambda(E_{\bar{\nu}_e}) = \delta(E_{\bar{\nu}_e} - E'_{\bar{\nu}_e})$:

$$\Psi(E_{\bar{\nu}_e}) = \frac{N_{90}}{N_{\text{T}} \sigma(E_{\bar{\nu}_e}) \sum_{k=1}^{k=4} \epsilon_{\text{live}}^k N_{\text{GRB}}^k \epsilon_s^k(E_{\bar{\nu}_e})}. \qquad (6)$$

The results of Equation (6) for the LGRBs (thin solid blue line), SGRBs (thin dashed blue line), and combined sets (thick blue line) are presented in Figure 2. We find the combined upper limit reaches a minimum of approximately 3.2×10^4 cm^{-2} at $E_{\bar{\nu}_e} = 100$ MeV. This result represents the world's most stringent limits for $\bar{\nu}_e$ energies below 17.5 MeV. The sensitivities of this measurement are found to be 2.3, 1.4, and 2.7 times larger than the observed limits for the LGRBs, SGRBs, and combined sets, respectively. The improvement over the previous KamLAND result (Asakura et al. 2015), represented by the solid and dashed
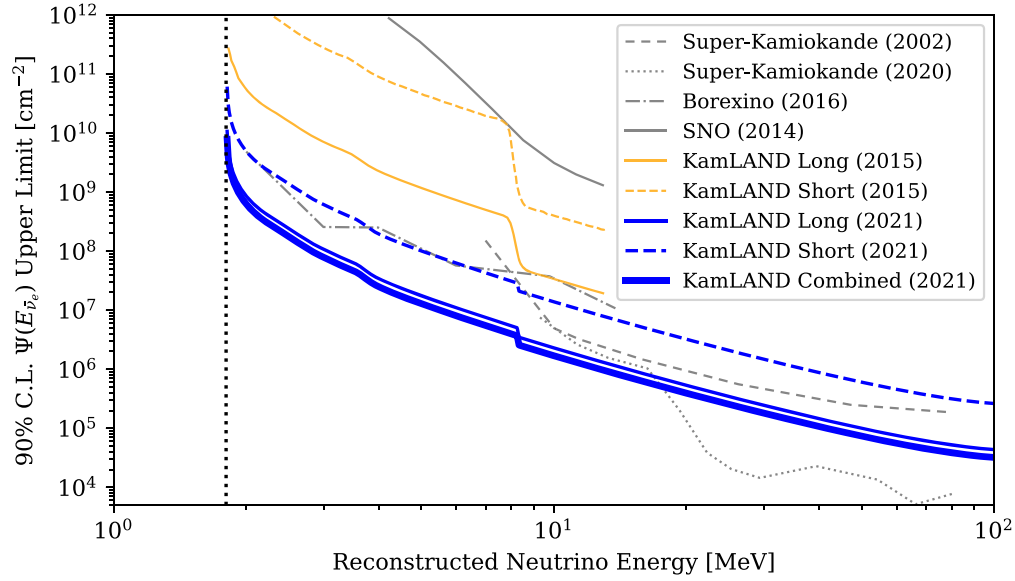
Figure 2. The 90% C.L. $\bar{\nu}_e$ fluence limit Green's function as a function of neutrino energy. The GRB combined set, shown in thick solid blue line, is compared to results from Super-Kamiokande (Fukuda et al. 2002; Orii et al. 2021), Borexino (Agostini et al. 2017), and SNO (Aharmim et al. 2014). Below 17.5 MeV, KamLAND establishes the tightest limits on $\bar{\nu}_e$ fluence. The slight distortion around $E_{\bar{\nu}_e} \approx 3$ MeV results from the energy dependence of the likelihood selection efficiency. Similarly, the bump at $E_{\bar{\nu}_e} \approx 8.3$ MeV comes from the prompt energy cut introduced in Period I. This figure also shows the LGRB and SGRB upper limits in thin solid and dashed blue lines, to be compared to the previous KamLAND result shown in orange. A vertical dotted line is shown at 1.8 MeV, the low-energy IBD threshold.

orange lines, originates from the increase in GRB statistics and the under-fluctuation in the background.

5.1. Source $\bar{\nu}_e$ Luminosity–Temperature Constraints

We now use N_{90} and the subset of GRBs with a measured redshift, z, to constrain the $\bar{\nu}_e$ integrated luminosity, L, and effective $\bar{\nu}_e$ temperature, T. The $\bar{\nu}_e$ spectrum from a single source can be written in terms of a luminosity as

$$\psi(E_{\bar{\nu}_e}, T, L)_{\rm FD} = \frac{L}{\langle E \rangle} \lambda(E_{\bar{\nu}_e}, T)_{\rm FD}. \quad (7)$$

The expected total flux at the detector in period k is therefore

$$\Psi^k(E_{\bar{\nu}_e}, T, L) = \sum_i^{i \in k} \frac{1 + z_i}{4\pi d_i^4} \psi((1 + z_i)E_{\bar{\nu}_e}, T, L), \quad (8)$$

where z_i and d_i are the redshifts and luminosity distances to the ith GRB. The $\bar{\nu}_e$ effective temperature and luminosity upper limits ($T_{\rm up}$, $L_{\rm up}$) are then connected to N_{90} through

$$N_{90} = N_T \sum_{k=1}^{k=4} \int_{E_{\rm low}^k}^{E_{\rm high}} \epsilon_{\rm live}^k \epsilon_s^k(E_{\bar{\nu}_e}) \sigma$$
$$\times (E_{\bar{\nu}_e}) \Psi^k(E_{\bar{\nu}_e}, T_{\rm up}, L_{\rm up}) dE_{\bar{\nu}_e}, \quad (9)$$

where $E_{\rm high} = 100$ MeV for $k = $ Periods I–IV, $E_{\rm low}^k = 1.8$ MeV for k in Periods II–IV, and 8.3 MeV for Period I. The $\bar{\nu}_e$ source luminosity upper limit at a given effective temperature is plotted in Figure 3 (left). This figure also includes the 68% C.L. compatible regions (red) from the observed neutrinos from SN 1987A; these measurements originate from the Kamiokande-II[24] (Hirata et al. 1988), Irvine-Michigan-Brookhaven (IMB;

---

[24] It has been suggested that the Kamiokande-II observation of SN 1987A is perhaps a factor of 2 low due to an unrecognized tape drive error and reset problem, which may have caused the much-discussed 7.3 s gap in the Kamiokande-II data. If correct, this would make the overlap with the IMB and Baksan data more consistent. See Oyama (2021).
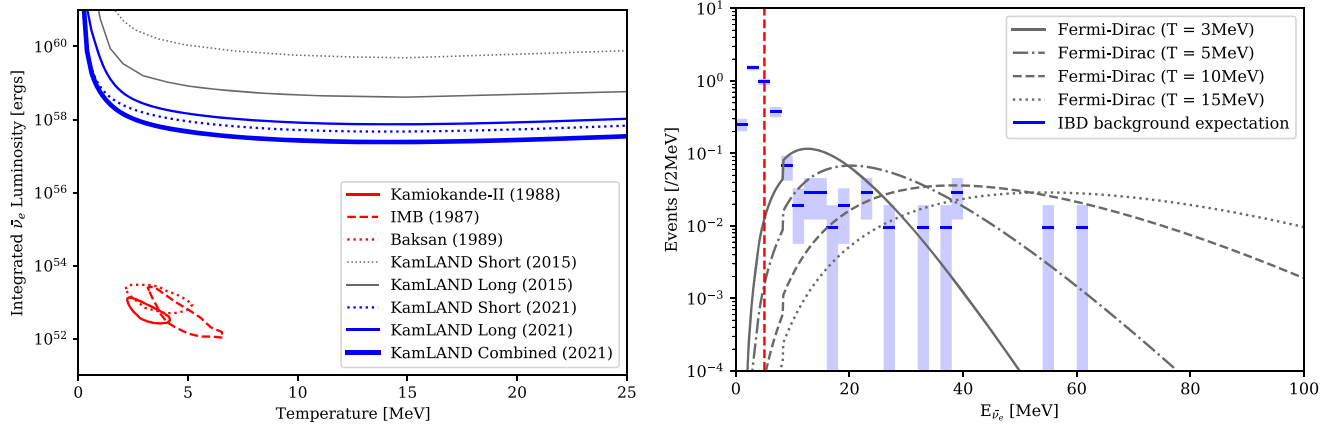
Schramm 1987), and Baksan (Lattimer & Yahil 1989) experiments.

Figure 3 (right) shows the expected background spectra (blue histogram) from the four KamLAND periods. We also include the shape of the FD neutrino spectrum at $T_{\rm up} = 3$, 5, 10, and 15 MeV, with the corresponding luminosity, $L_{\rm up}$, from Equation (9).

As noted in Section 1, GRB 170817A was determined to be in the class SGRB. Because this event is also the closest observed GRB, $\approx$40 Mpc, it also is the dominant contribution to the limit calculated through Equation (9). We therefore placed this event into the SGRB class for this analysis. It has been noted that GRB 170817A also lacks the hard spectrum of an SGRB and may indicate additional classes or subclasses in the current GRB classification scheme (Horváth et al. 2018).

The results presented here assume an isotropic neutrino emission from the source; however, the accretion disk and remnant are expected to radiate neutrinos preferentially along the polar direction (Perego et al. 2014). Even so, the limits indicate that KamLAND should not expect any significant correlated observation until the observation of a GRB localized to the Milky Way or one of the Milky Way's satellite galaxies within $\sim$0.5 Mpc. We also note that the calculations do not incorporate neutrino oscillations or other flavor-changing effects that could either increase or decrease the number of neutrinos observed by KamLAND.

If a GRB is localized within $\sim$0.5 Mpc, a future search should be conducted on that individual source rather than performing a stacked analysis, as was performed here. If the background expectation in the search time window is below 0.50 (0.12) events, a single coincident observation would yield a nonzero 90% (99%) C.L. lower limit on the electron antineutrino flux. If this analysis is repeated with a significantly larger detector, and thus a larger background expectation, the limits can be determined separately for each energy bin, as in Orii et al. (2021). Alternatively, a low-energy cutoff at $\sim$7.5 MeV can be placed, as we have done for Period I, to

Figure 3. Left: the constraint on the $\bar{\nu}_e$ source luminosity and effective temperature relation in terms of LGRB (thin solid blue line), SGRB (dotted blue line), and the combined sets (thick solid blue line). The SN 1987A neutrino measurements from the Kamiokande-II (Hirata et al. 1988), IMB (Schramm 1987), and Baksan (Lattimer & Yahil 1989) experiments are shown in solid, dashed, and dotted closed red contours, respectively. Right: The $\bar{\nu}_e$ energy distribution background expectation throughout the four KamLAND periods are shown in blue with the 1σ statistical errors. Assuming an FD neutrino energy distribution from the GRB source, we show the 90% C.L. upper limit at 3, 5, 10, and 15 MeV $\bar{\nu}_e$ source temperatures. The vertical dashed red line corresponds to the energy of the single observed coincident event.

reduce the reactor neutrino background. The background estimation for these analyses will also benefit from tighter constraints on the predefined window size t_p. This will primarily be influenced by revised limits on the sum of the neutrino masses or a measurement of an effective neutrino mass and by potentially theoretical model-dependent time differences between the neutrino and photon production. Finally, if the GRB happens to occur nearby, a separate search for the less likely neutral current $\bar{\nu}_e$ interaction with ^{12}C at 15 MeV could be performed with very low background levels, expected to be dominated by atmospheric neutrino interactions.

6. Conclusion

This paper presents a time-coincident search for low-energy $\bar{\nu}_e$ in the KamLAND detector with 2795 LGRBs and 465 SGRBs. We search for events between the first GRB 2004 December 19 and the most recent KamLAND run in 2021 June 12 using a GRB catalog compiled from the GCN and GBM. With a time window of ±500 s around each GRB plus the GRB event duration, we find a single candidate $\bar{\nu}_e$ coincident event. This observation is not statistically significant. From this, we present an upper limit on the $\bar{\nu}_e$ fluence, placing the most stringent limit below 17.5 MeV. Finally, using the known redshifts in the subset of GRBs, we assume an FD energy spectrum to place a limit on the $\bar{\nu}_e$ luminosity and effective temperature.

ORCID iDs

T. Hachiya https://orcid.org/0000-0002-4238-7990
K. Ichimura https://orcid.org/0000-0001-9783-5781
S. Ieki https://orcid.org/0000-0001-7694-1921
K. Ishidoshiro https://orcid.org/0000-0001-9271-2301
N. Kawada https://orcid.org/0000-0003-2350-2786
J. Shirai https://orcid.org/0000-0002-3988-2309
H. Watanabe https://orcid.org/0000-0002-2363-5637
S. Obara https://orcid.org/0000-0003-3488-3553
B. K. Fujikawa https://orcid.org/0000-0002-7001-717X
S. N. Axani https://orcid.org/0000-0001-8866-3826
A. Li https://orcid.org/0000-0002-4844-9339
M. P. Decowski https://orcid.org/0000-0002-1577-6229

References

Abbasi, R., Abdou, Y., Abu-Zayyad, T., et al. 2009, ApJ, 701, 1721
Abbasi, R., Abdou, Y., Abu-Zayyad, T., et al. 2010, ApJ, 710, 346
Abbott, B. P., Abbott, R., Abbott, T., et al. 2017b, PhRvL, 119, 161101
Abbott, B. P., Abbott, R., Abbott, T. D., et al. 2017a, ApJL, 848, L12
Abe, S., Asami, S., Gando, A., et al. 2021, ApJ, 909, 116
Abe, S., Asami, S., Gando, A., et al. 2022a, ApJ, 924, 103
Abe, S., Asami, S., Gando, A., et al. 2022b, ApJ, 925, 14
Abe, S., Ebihara, T., Enomoto, S., et al. 2008, PhRvL, 100, 221803
Abe, S., Enomoto, S., Furuno, K., et al. 2010, PhRvC, 81, 025807
Aghanim, N., Akrami, Y., Ashdown, M., et al. 2020, A&A, 641, A6
Agostini, M., Altenmüller, K., Appel, S., et al. 2017, APh, 86, 11
Aguilar, J. A. 2011, in Proc. of the 32nd Int. Cosmic Ray Conf. (ICRC2011)
  (Trieste: PoS)
Aharmim, B., Ahmed, S., Anthony, A., et al. 2014, APh, 55, 1
Albert, A., André, M., Anghinolfi, M., et al. 2017, MNRAS, 469, 906
Araki, T., Enomoto, S., Furuno, K., et al. 2005, Natur, 436, 499
Asakura, K., Gando, A., Gando, Y., et al. 2015, ApJ, 806, 87
Avrorin, A., Aynutdinov, V., Belolaptikov, I., et al. 2011, AstL, 37, 692
Burns, E. 2020, LRR, 23, 1
Chrimes, A., Levan, A., Stanway, E., et al. 2019, MNRAS, 488, 902
Esteban, I., González-García, M. C., Maltoni, M., Schwetz, T., & Zhou, A.
  2020, JHEP, 2020, 178
Feldman, G. J., & Cousins, R. D. 1998, PhRvD, 57, 3873
Fukuda, S., Fukuda, Y., Ishitsuka, M., et al. 2002, ApJ, 578, 317
Gando, A., Gando, Y., Hachiya, T., et al. 2016a, ApJL, 829, L34
Gando, A., Gando, Y., Hachiya, T., et al. 2016b, PhRvL, 117,
  082503
Gando, A., Gando, Y., Hanakago, H., et al. 2013, PhRvD, 88, 033001
Gando, Y., Gando, A., Hachiya, T., et al. 2020, JPhCS, 1468, 012142
Gando, Y., Gando, A., Hachiya, T., et al. 2021, JInst, 16, P08023

Gando, Y. 2020, JPhCS, 1468, 012142

Hirata, K., Kajita, T., Koshiba, M., et al. 1988, PhRvD, 38, 448

Horiuchi, S., Beacom, J. F., & Dwek, E. 2009, PhRvD, 79, 083013

Horváth, I., Tóth, B., Hakkila, J., et al. 2018, Ap&SS, 363, 1

Hughey, B., & Taboada, I. 2005, arXiv:0509570

Kim, Y., & Im, M. 2012, Bull. Korean Astron. Soc., 37, 82.1

Kouveliotou, C., Meegan, C. A., Fishman, G. J., et al. 1993, ApJL, 413, L101

Lattimer, J. M., & Yahil, A. 1989, ApJ, 340, 426

Lazzati, D. 2005, MNRAS, 357, 722

Liu, B., Meyer, F., & Meyer-Hofmeister, E. 1996, Astronomische Gesellschaft Abstract Series, 12, 189

Nakar, E. 2007, PhR, 442, 166

Orii, A., Abe, K., Bronner, C., et al. 2021, PTEP, 2021, 103F01

Oyama, Y. 2021, ApJ, 922, 223

Ozaki, H., & Shirai, J. 2017, in 38th Int. Conf. on High Energy Physics (ICHEP2016) (Trieste: PoS)

Perego, A., Rosswog, S., Cabezón, R. M., et al. 2014, MNRAS, 443, 3134

Rosswog, S., & Liebendoerfer, M. 2003, MNRAS, 342, 673

Ruffert, M., & Janka, H.-T. 2001, A&A, 380, 544

Schramm, D. N. 1987, CoNPP, 17, 239

Setiawan, S., Ruffert, M., & Janka, H.-T. 2006, A&A, 458, 553

Strumia, A., & Vissani, F. 2003, PhLB, 564, 42

Totani, T., Sato, K., Dalhed, H., & Wilson, J. 1998, ApJ, 496, 216

Xu, D., de Ugarte Postigo, A., Leloudas, G., et al. 2013, ApJ, 776, 98